The Astrophysical Journal, 912:153 (15pp), 2021 May 10 https://doi.org/10.3847/1538-4357/abf42d

He I 10830 Å Dimming during Solar Flares. I. The Crucial Role of Nonthermal Collisional Ionizations

Graham S. Kerr[1,2], Yan Xu[3,4], Joel C. Allred[1], Vanessa Polito[5,6], Viacheslav M. Sadykov[7], Nengyi Huang[3], and Haimin Wang[3,4]

[1] NASA Goddard Space Flight Center, Heliophysics Sciences Division, Code 671, 8800 Greenbelt Road, Greenbelt, MD 20771, USA; graham.s.kerr@nasa.gov, kerrg@cua.edu
[2] Department of Physics, Catholic University of America, 620 Michigan Avenue, Northeast, Washington, DC 20064, USA
[3] Institute for Space Weather Sciences, New Jersey Institute of Technology, 323 Martin Luther King Boulevard, Newark, NJ 07102-1982, USA
[4] Big Bear Solar Observatory, New Jersey Institute of Technology, 40386 North Shore Lane, Big Bear City, CA 92314-9672, USA
[5] Bay Area Environmental Research Institute, NASA Research Park, Moffett Field, CA 94035-0001, USA
[6] Lockheed Martin Solar and Astrophysics Laboratory, Building 252, 3251 Hanover Street, Palo Alto, CA 94304, USA
[7] Physics & Astronomy Department, Georgia State University, 25 Park Place NE, Atlanta, GA 30303, USA
Received 2021 March 5; revised 2021 March 29; accepted 2021 March 30; published 2021 May 17

Abstract

While solar flares are predominantly characterized by an intense broadband enhancement to the solar radiative output, certain spectral lines and continua will, in theory, exhibit flare-induced dimmings. Observations of transitions of orthohelium He I $\lambda\lambda$ 10830 Å and the He I D3 lines have shown evidence of such dimming, usually followed by enhanced emission. It has been suggested that nonthermal collisional ionization of helium by an electron beam, followed by recombinations to orthohelium, is responsible for overpopulating those levels, leading to stronger absorption. However, it has not been possible observationally to preclude the possibility of overpopulating orthohelium via enhanced photoionization of He I by EUV irradiance from the flaring corona followed by recombinations. Here we present radiation hydrodynamics simulations of nonthermal electron-beam-driven flares where (1) both nonthermal collisional ionization of helium and coronal irradiance are included, and (2) only coronal irradiance is included. A grid of simulations covering a range of total energies deposited by the electron beam and a range of nonthermal electron-beam low-energy cutoff values were simulated. In order to obtain flare-induced dimming of the He I 10830 Å line, it was necessary for nonthermal collisional ionization to be present. The effect was more prominent in flares with larger low-energy cutoff values and longer lived in weaker flares and flares with a more gradual energy deposition timescale. These results demonstrate the usefulness of orthohelium line emission as a diagnostic of flare energy transport.

Unified Astronomy Thesaurus concepts: Active solar chromosphere (1980); Solar chromosphere (1479); Solar physics (1476); Solar flares (1496); Solar flare spectra (1982); Spectroscopy (1558); Radiative transfer simulations (1967); Hydrodynamical simulations (767); Solar radiation (1521)

1. Introduction

The intense broadband enhancement to the solar radiative output, following deposition of tremendous amounts of energy released during magnetic reconnection, is what characterizes solar flares. As well as these brightenings, models of flare radiation have suggested that there may be flare-induced dimmings at certain wavelengths. Typically these concern the Balmer and Paschen continua and are known as "black-light flares" (BLF) or "negative flares". Despite their modest magnitude and transient nature, BLFs may be a powerful means to constrain the magnitude, temporal profile, spectral properties, and mechanism of energy transported from the coronal release site through the transition region (TR) and chromosphere. The strength and duration of such dimmings depend on the magnitude of energy deposited, but they are typically thought to be transient and difficult to observe due to their small contrast. Indeed, no unambiguous continuum BLF has been observed (e.g., Henoux et al. 1990; van Driel-Gesztelyi et al. 1994; Ding et al. 2003). On the other hand, a similar phenomenon has been convincingly observed in solar and stellar flare spectra of orthohelium (see discussion below)—that is, flare-induced dimmings of the He I 10830 Å and He I D3 lines.

In the standard model of solar flares, the bulk of the flare energy is transported by a directed beam of nonthermal electrons, accelerated out of the ambient thermal background during magnetic reconnection. As these electrons propagate at relativistic speeds through the solar atmosphere, they lose energy primarily via Coulomb collisions, ultimately thermalizing in the chromosphere or TR. Hard X-ray bremsstrahlung is observed at the site of thermalization, in compact footpoint sources, from which the properties of the nonthermal electron distribution can be inferred (e.g., Holman et al. 2011). The chromospheric and TR plasma rapidly heats and ionizes, and strong mass flows develop chromospheric ablations (upward flows, also referred to as evaporation) and condensations (dense, downward-directed flows).

In addition to heating the plasma, the precipitating nonthermal electrons (or protons, or other ions) can collisionally excite or ionize the target atoms or ions, referred to as nonthermal collisional ionization/excitation, C_{nt}. It has been known for some time that nonthermal effects are important for the response of hydrogen continua and spectral line transitions (e.g., Aboudarham & Henoux 1986; Fang et al. 1993; Kašparová et al. 2009, and references therein). Forward models of hydrogen continua in flares have shown that brief dimmings may result due to the increased population of excited states following nonthermal collisional excitation of hydrogen, increasing the absorption of photospheric photons (e.g., Henoux et al. 1990; Abbett & Hawley 1999).

While there is a lack of convincing observations of continuum BLFs, spectral transitions of orthohelium have shown convincing evidence of dimming, with the appearance of "negative" flare ribbons—that is, the background-subtracted emission in flares is weaker than the preflare emission, with an enhanced absorption line profile. A remarkable flare observation in the He D3 line at 5876 Å was carried out by Dr. Zirin (Zirin 1980) on 1978 July 10 at Big Bear Solar Observatory (BBSO). A dark shell in the He I D3 line was observed at the very beginning of the flare and eventually turned to emission. Later on, using digitized film data, Liu et al. (2013) reported an M6.3 flare on 1984 May 22 with an initial dimming of about 5% in He I D3 that persisted for four minutes.

In the He I 10830 Å line, the emission has usually been observed during flares (e.g., You & Oertel 1992; Penn & Kuhn 1995; Penn 2000; Li et al. 2006; Liu et al. 2013; Zeng et al. 2014). There is a correlation between the intensity of the line and the X-ray flux, and emission only appears in moderate-to-strong flares. This threshold is not definitively known but seems to be around mid-C class (Li et al. 2007; Du & Li 2008).

Though rare, He I 10830 Å dimmings have now been observed in several flares. For example, Harvey & Recely (1984) presented observations of persistent dark flare ribbons during a long-duration event. More recently, Xu et al. (2016) found dimmings on the leading edge of the propagating ribbons in two M-class flares using the 1.6 m GST/BBSO (Goode & Cao 2012) observations that have provided the highest spatial resolutions so far. Their observations were carried out using a Lyot filter (Cao et al. 2010) tuned to the blue wing (10830.05 Å ± 0.25 Å) and showed dimming of the leading edge of the flare ribbon. The dark ribbon front observed in He I 10830 Å had a characteristic width of ≈350–500 km, with a dimming up to 13.7%. Simultaneously, blue-wing-enhanced Hα emission and significantly broadened Mg II h & k lines, which retained their central reversal, were observed at the same location where He I 10830 Å darkening is seen. Enhanced absorption was confined to the propagating ribbon front, the presumed site of energy injection at the base of newly reconnected magnetic flux loops, and persisted for several tens to over a hundred seconds before turning into a positive contrast. This positive contrast was associated with the trailing region of the flare ribbons. Spectroscopic observations of a small flare (of B2 class) were analyzed by Kobanov et al. (2018), who saw only enhanced absorption of up to 25%, appearing in two minima but with no subsequent increase in emission. Asymmetries and Doppler shifts were detected along with increases in line width.

Stellar flare observations of 10830 Å are even rarer than the solar case but demonstrate similar patterns. In M-dwarf flare stars, He I 10830 Å is generally in emission (Schmidt et al. 2012), strongly broadened, and asymmetric (Fuhrmeister et al. 2020). A strong flare response in He I 10830 Å was typically accompanied by broad, asymmetric Hα profiles (Fuhrmeister et al. 2020). There has now been a detection of enhanced He I 10830 Å absorption observed at the onset of M-dwarf flares using data from the CARMENES study (Fuhrmeister et al. 2020). When He I 10830 Å was undergoing flare-induced dimming, the Hα showed a modest response coupled with a blue-wing asymmetry.

Transitions in the triplet state of He I (orthohelium) form the 10830 and D3 lines. He I 10830 Å is a self-blend of three transitions closely spaced in wavelength, from He I 2 s $^3S_1 \rightarrow 2p^3P_{2,1,0}$ transitions. The He I D3 lines are a multiplet of lines near 5875 Å from the He I $2p^3P_{2,1,0} \rightarrow 3d^3D_{3,2,1}$ transitions. They generally appear in absorption in the quiet Sun (Andretta & Jones 1997), but have been observed to go into emission during flares as described above, or in more localized heating events (see Libbrecht et al. 2019, 2020 and references therein). The excitation energy between the ground and lower level of the triplet is ∼20 eV, meaning that thermal electron collisions in the chromosphere are unable to directly populate orthohelium (we refer to this as the thermal collisional mechanism, CM). Without a sufficiently large population of orthohelium to absorb photospheric 10830 Å photons, the strong absorption line that is observed cannot form. This led Goldberg (1939) to propose the photoionization of He I followed by recombinations to orthohelium as a population mechanism. This is known as the photoionization–recombination mechanism (PRM). The source of $\lambda < 504$ Å photons is the extreme ultraviolet (EUV) and soft X-ray emission from the hot overlying corona, which irradiates the chromosphere. He I 10830 Å is therefore a good tracer of coronal activity. Extensive modeling and observations have confirmed the PRM as the dominant pathway to populating orthohelium in the quiet Sun (e.g., Zirin 1975; Avrett et al. 1994; Andretta & Jones 1997; Centeno et al. 2008; Leenaarts et al. 2016).

To explain flare observations of He I 10830 Å and He I D3 dimming, it has been speculated that the PRM becomes enhanced during the flare. Coronal EUV irradiance would increase due to heating and chromospheric ablation, which substantially raises the emission measure, leading to excess helium ionization over the preflare state. Overpopulated orthohelium would proceed to absorb more 10830 Å photons, strengthening the absorption line. Once the plasma becomes sufficiently hot and dense, thermal collisions drive the line into emission. This mechanism has been used to interpret solar and stellar flare observations of orthohelium (e.g., Zeng et al. 2014; Kobanov et al. 2018; Fuhrmeister et al. 2020).

An alternative idea to the PRM is that nonthermal collisional ionization of helium is responsible for the negative flares (Ding et al. 2005). Nonthermal ionization of He I → He II followed by recombinations to orthohelium would overpopulate those levels relative to the preflare, with absorption and emission of orthohelium lines occurring as described before. We refer to this mechanism as the nonthermal collisional–recombination mechanism (CRM). CRM would demand the presence of a nonthermal electron distribution in the chromosphere during the flare (e.g., from bombardment by a beam of accelerated electrons), the properties of which would affect the magnitude and duration of dimming and enhancement. PRM would not require accelerated electrons but simply a flare-heated, mass-loaded corona. It is important to note that coronal irradiance would occur in both models, as regardless of the flare energy transport mechanism, the corona is heated.

There have been relatively few forward-modeling attempts of orthohelium in solar or stellar flares, but past modeling has yielded interesting results. Using semiempirical flare atmospheres, Ding et al. (2005) simulated the effect of including nonthermal collisional ionization on He I 10830 Å. Applied to the VAL-C atmosphere (Vernazza et al. 1981), these

nonthermal collisions led to enhanced absorption, and in the semiempirical flare atmospheres F1 & F2 (Machado et al. 1980), the simulations with nonthermal collisions resulted in increased emission over the simulations without C_{nt}. However, while they included EUV radiation from the corona, this was not time dependent, and those authors could not fully model both CRM and PRM in a realistic manner simultaneously. Huang et al. (2020) considered both CRM and PRM in realistic time-dependent RADYN simulations of electron-beam-driven flares produced by the F-CHROMA consortium.[8] The implementation of these methods is described below. They did find enhanced absorption in He I 10830 Å emission and found some simulations with contrasts similar to observed ones, albeit much shorter lived. However, Huang et al. (2020) did not separate the effects of each mechanism, meaning it is not clear if the dominant role is CRM or PRM.

Having previously confirmed that our state-of-the-art electron-beam-driven flare radiation hydrodynamic models can exhibit He I 10830 Å dimming (Huang et al. 2020), we can now determine if the inclusion of CRM is strictly necessary or if PRM alone can produce enhanced absorption. Determining if CRM is indeed the dominant mechanism is the first step in utilizing helium negative flares to diagnose energy transport in both solar and stellar flares. One set of experiments presented here includes both the CRM and PRM methods; the other only includes PRM. The impact on He I 10380 Å is determined in each case.

2. Numerical Experiments

2.1. The RADYN code and Modeling Helium in Flares

To explore the response (this work) and formation properties (to appear in a forthcoming work) of the He I 10830 Å line during solar flares, we employ the radiation hydrodynamics (RHD) code RADYN (Carlsson & Stein 1992, 1995, 1997; Allred et al. 2005, 2015), which is ideally suited for such a study. Nonequilibrium atomic level populations and ionization of hydrogen, helium, and calcium are included, as are photoionizations from coronal irradiation of the chromosphere. Both of these processes are known to be important to accurately consider helium ionization stratification and in populating orthohelium (e.g., Goldberg 1939; Avrett et al. 1994; Andretta & Jones 1997; Golding et al. 2014, 2016; Leenaarts et al. 2016). Nonthermal collisional ionization of helium is also included in our simulations so that both the PRM and CRM methods of populating orthohelium are considered. RADYN is a well-established resource that has been used to investigate flare atmospheric dynamics, the radiative response to flares, and to understand energy transport processes in both solar and stellar flares (recent examples include Kowalski et al. 2015, 2017; Rubio da Costa et al. 2016; Kerr et al. 2016, 2019b, 2020; Simões et al. 2017; Brown et al. 2018; Polito et al. 2018, 2019; Huang et al. 2020) Some pertinent points are listed here, but for full details of RADYN, in particular the flare versions, consult Abbett & Hawley (1999) and Allred et al. (2005, 2015). RADYN is a one-dimensional magnetic field field-aligned RHD numerical model, with an adaptive grid (Dorfi & Drury 1987), enabling the resolution of shocks and strong gradients that typically form in flare simulations.

[8] https://star.pst.qub.ac.uk/wiki/doku.php/public/solarmodels/start

Helium is included as a nine-level-with-continuum atom, with the ground states of He I, He II, and He III, and various excited states. The upper and lower levels of the He I 10830 Å line are included, but the sublevels of the ^3P state are modeled as a single level, with the statistical weight equal to the sum of the weights of the sublevels. This means only one component of the triplet is forward modeled, which is sufficient for this study. A future study will investigate the full triplet as well as the He I D3 lines. Photoionizations–recombinations (bound-free transitions) from both the ground and excited states are included. RADYN does not include overlapping bound–bound transitions.

Optically thin losses are included by summing the emissivity of all transitions from the CHIANTI (V7.1.3; Dere et al. 1997; Landi et al. 2013) atomic database (apart from those transitions included in the detailed radiation transfer). Half of the optically thin losses are directed downwards, and act to heat or ionize the denser layers of the atmosphere. Emissivities from CHIANTI were tabulated on a wavelength and temperature grid, and are the product of the emissivities and emission measures integrated through the TR and coronal portion of the loop. This is then included as a downward-directed source of irradiation when solving the radiation transfer problem, in the manner described by Wahlstrom & Carlsson (1994) and in Allred et al. (2015). We can therefore account for the time-varying EUV irradiation of the chromosphere during the flare, which affects the formation of He I 10830 Å.

To model solar flares, a nonthermal electron distribution (described by a power-law energy spectrum with total instantaneous flux $F_{\rm ins}$ above a low-energy cutoff E_c, with spectral slope δ) is injected at the apex of the loop, which propagates at relativistic speeds through the atmosphere. The atmosphere consists of a subphotosphere, photosphere, chromosphere, TR, and corona, with a total height (a loop half-length) of $z \approx 11$ Mm. The preflare atmosphere was in radiative equilibrium, with a coronal temperature and electron density of $T \approx 3.15$ MK and $n_e \approx 7.6 \times 10^9$ cm^{-3}. This version of RADYN uses a new code, FP (Allred et al. 2020), to model the evolution of this distribution as it is transported through the plasma, by solving the Fokker–Planck equations, an update from Allred et al. (2015). Importantly, we make no assumption about the temperature of the target onto which the electrons precipitate. That is, we do not need to assume either a warm or a cold target, the actual temperature of the plasma is used in our solution. FP can act either as a standalone code or can be merged with RHD codes as we have done here with RADYN. It is a marked improvement over prior efforts, and we encourage the reader to consult Allred et al. (2020) to learn more about this open-source code. Nonthermal collisional ionizations and excitations from the ground state of hydrogen are included using the formalism of Fang et al. (1993). nonthermal collisional ionization from the ground state of He I $\rightarrow$ He II, and from the ground state of He II $\rightarrow$ He III are included by integrating the product of the collisional cross-sections σ_{ij} and the nonthermal electron energy distribution function $v_b f$, over energy, E, and pitch angle μ:

$$C_{nt} = 2\pi \int \int \mu v_b f \sigma_{ij} dE d\mu. \quad (1)$$

Parameterized values of σ_{ij} as functions of electron energy were obtained from Arnaud & Rothenflug (1985). This differs from the approach of Ding et al. (2005), who instead assumed that the He C_{nt} could be obtained from the hydrogen rates

$C_{nt,\ \mathrm{hyd}}$ multiplied by the ratio of helium to hydrogen cross-sections at 30 keV: $C_{nt} = \sigma_{\mathrm{He}}/\sigma_H\, C_{nt,\ \mathrm{hyd}} = 1.2 C_{nt,\ \mathrm{hyd}}$. It is unclear to us which method is most appropriate, and so we elected to keep using the Arnaud & Rothenflug (1985) rates that have been employed by RADYN since Allred et al. (2015). This also lets us model C_{nt} of He I $\rightarrow$ He II $\rightarrow$ He III, whereas Ding et al. (2005) only considered C_{nt} of He I $\rightarrow$ He II.

2.2. Flare Simulations

A grid of fifty nonthermal electron-beam-driven flare simulations were produced using RADYN, where we varied the magnitude of total energy flux (F_{tot} erg cm^{-2}) injected, the timescale of energy injection (τ_{injs}), so that the instantaneous energy flux (F_{ins} erg cm^{-2} s^{-1}) varied even for simulations with the same F_{tot} and the low-energy cutoff of the distribution (E_{c} keV). The spectral index $\delta = 5$ was fixed. This allowed a range of flare strengths and spectral energy distributions to be studied. We vary the energy distribution by varying the low-energy cutoff of the distribution. A larger low-energy cutoff means that there are more high-energy electrons that can penetrate deeper into the chromosphere (because low-energy electrons thermalize at smaller column depths). We note that the descriptors of "hard" or "soft" nonthermal electron distributions generally refer to variations of δ because energy is distributed toward higher or lower energy electrons, respectively. However, in this work, we refer to a "harder" spectrum as simulations with larger values of E_c because there are more high-energy electrons compared to "softer" spectra with more low-energy electrons. We used five values of E_c in our experiments: $Ec = [10,\ 15,\ 20,\ 25,\ 30]$ keV. These experiments were repeated with nonthermal collisional ionizations of helium omitted, giving 100 simulations in total.

The total injected energy fluxes were $F_{\mathrm{total}} = [1 \times 10^{10},\ 5 \times 10^{10},\ 1 \times 10^{11},\ 5 \times 10^{11},\ 1 \times 10^{12}]$ erg cm^{-2}. Hereafter, the notation *XFY* means $F_{\mathrm{total}} = X \times 10^{Y}$ erg cm^{-2} (this differs somewhat from other uses of *XFY* in the flare-modeling literature where this typically refers to the instantaneous energy flux, but because we are comparing injection timescales, we focus on the total energy flux). Those fluxes were injected either over $\tau_{\mathrm{inj}} = [10,\ 20]$ s. The former means that the instantaneous energy flux F_{ins} was constant, the latter means that F_{ins} ramped up to a peak at $t = 10$ s then decreased in a triangular profile. Once heating ceased the experiments ran to $t = 50$ s.

Examples illustrating the differences in the atmospheric response that arise from varying the injection timescale or spectral hardness of the electron distribution are shown in Figure 1. The temperature and electron density stratification at 1.5 s cadence for the first 30 s of the 1F11 simulations are shown for $\tau_{\mathrm{inj}} = 10$ s (panels A,B,E,F) and $\tau_{\mathrm{inj}} = 20$ s (panels C,D,G,H). The left-hand column has $E_{\mathrm{c}} = 10$ keV (softest distribution), and the right-hand one has $E_{\mathrm{c}} = 30$ keV (hardest distribution). While both heating durations (10 s or 20 s) ultimately produce fairly similar atmospheres by the end of their respective heating phases, the differences in the time taken to reach certain temperatures and electron densities will have a consequential impact on the radiative response. It is clear that the softer distributions strongly heat and ionize the upper chromosphere/lower TR due to the larger proportion of low-energy electrons that more easily thermalize at the low column depth. The harder distribution can penetrate a deeper, resulting in a lower magnitude of heating, but much wider swathe of the chromosphere significantly involved in the flare. This shifts the peak electron density deeper. The electron density enhancement is governed not only by the temperature response but, particularly at greater depth, by hydrogen $C_{nt,\mathrm{hyd}}$. Not shown

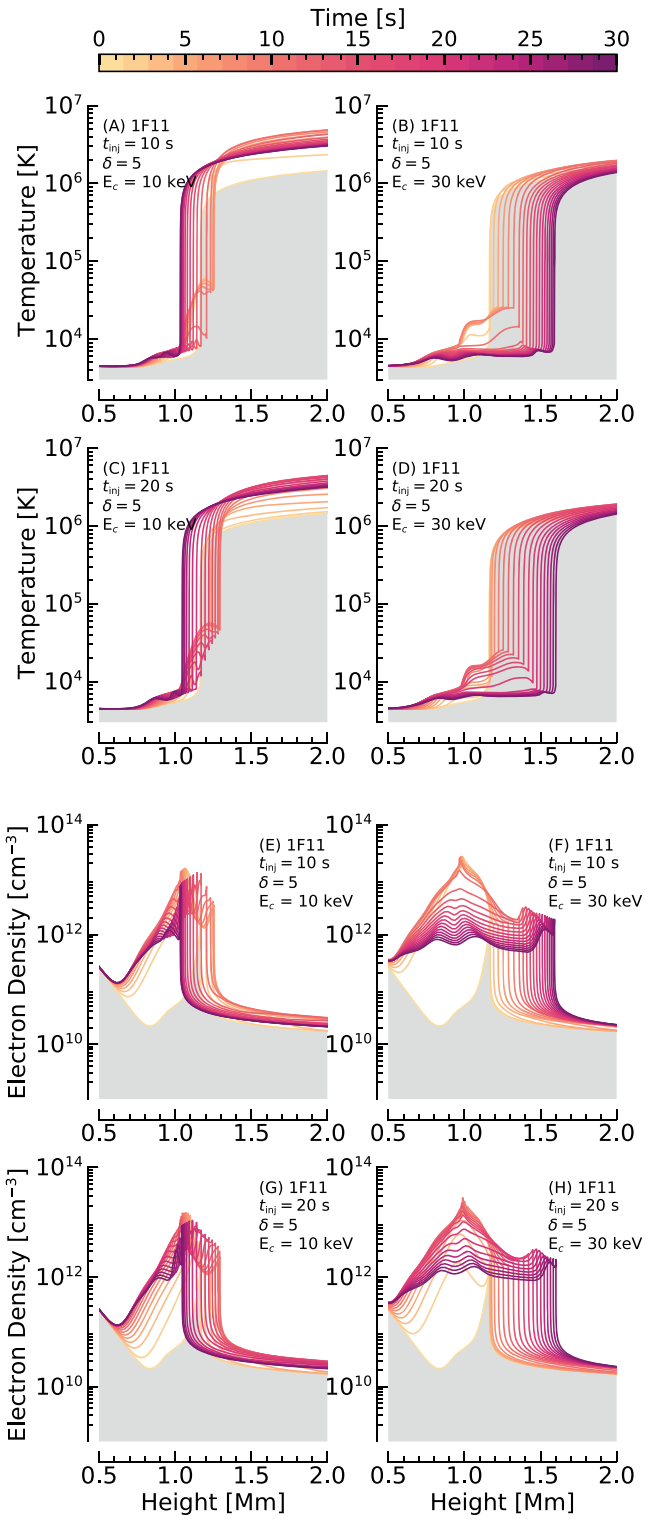

Figure 1. Temperature (top four panels) and electron density (bottom four panels) stratification as a function of time in the electron-beam-driven flare simulations. Total energy flux is 1×10^{11} erg cm^{-2} with $\delta = 5$. Panels (A, B, E, F) show the $\tau_{\mathrm{inj}} = 10$ s scenario, and panels (C, D, G, H) show $\tau_{\mathrm{inj}} = 20$ s. The simulations in the left-hand column have $E_{\mathrm{c}} = 10$ keV and in the right-hand column have $E_{\mathrm{c}} = 30$ keV. The grayscale shows the preflare stratification.

Table 1
Conduction-only Flare Simulations

	Total Energy Flux [erg s^{-1} cm^{-2}]	Energy Deposition Location
Exp. 1	2×10^{11}	Equally over 11 − 9 Mm
Exp. 2	2×10^{10}	Equally over 11 − 9 Mm
Exp. 3	2×10^{9}	Equally over 11 − 9 Mm
Exp. 4	1.4×10^{10}	Constant over 11 − 5 Mm then decreasing to zero between 5 − 3 Mm
Exp. 5	7×10^{9}	Constant over 11 − 5 Mm then decreasing to zero between 5 − 3 Mm
Exp. 6	1.4×10^{11}	Constant over 11 − 5 Mm then decreasing to zero between 5 − 3 Mm
Exp. 7	1.6×10^{11}	Equally over 11 − 3 Mm

are the velocities driven by energy injection, but in all experiments, there is an upflow that increases in magnitude with increasing flare energy, from a few $\times 10$ km s^{-1} to several $\times 100$ km s^{-1}. The higher energy simulations also drive downflows of a few $\times 10$ km s^{-1}, which occur more commonly in flares with softer nonthermal electron distributions. The experiments shown here all include He C_{nt}. Those that omit He C_{nt} are very similar with only subtle differences, likely due to the importance of He II 304 Å to radiative losses.

While the majority of this work discusses electron-beam-driven flares, we additionally performed seven experiments where energy was deposited directly in the corona and transported solely by the thermal conductive flux. Those experiments, listed in Table 1, were not designed to be comprehensive. Rather they serve to be illustrative of how direct in situ heating at the loop apex resulting from reconnection might result in coronal heating, thereby increasing the irradiation of the chromosphere, before the chromosphere itself is directly heated. The atmospheric stratification for experiments 1, 4, and 6 is shown in Figure 2. Gradients in the chromosphere are sharper than in the electron-beam simulations, with the TR being pushed to greater depth in each case. The flaring corona precedes the flaring chromosphere by several seconds. While the coronal temperature near the top of the loop increases rapidly, the density (therefore emission measure) takes longer as the corona is mass loaded by the evaporation of chromospheric material so it is only when the heat flux reaches the chromosphere that this commences.

2.3. Modeling He I 10830 Å with RADYN+RH

RADYN does not consider overlapping transitions, meaning that photoionizations of He I by the He II 304 Å line are not present. We can explore the importance of this effect using the RH radiation transfer code (Uitenbroek 2001). RH is a stationary code that solves the NLTE radiation transfer assuming statistical equilibrium for any species of interest. Overlapping transitions are included for those atomic species. Snapshots of RADYN flare atmospheres can be input to RH (using the NLTE nonequilibrium electron density from RADYN somewhat mitigates the use of statistical equilibrium) to forward-model radiation either not modeled by RADYN or to explore additional physical processes. Similar experiments have been performed extensively (e.g., Kerr et al. 2016; Rubio da Costa et al. 2016; Rubio da Costa & Kleint 2017; Zhu et al. 2019; Graham et al. 2020).

As standard, RH does not include coronal irradiation in the solution of the equation of radiative transfer nor does it include nonthermal collisional processes. Because PRM is the primary population mechanism for orthohelium in the quiet Sun, and because both the PRM and the CRM (as we demonstrate in this work) are vital in flares, we used a modified version of RH to model helium. Our implementation of coronal irradiation is described in Kerr et al. (2019a). Nonthermal collisional ionization rates for helium were saved for each snapshot of interest, written as a new input file to RH, and added to the thermal collisional ionization rates.

Snapshots of the 1F11 $\tau_{\rm inj} = 20$ s simulation at 0.1 s cadence were processed through RH, solving the NLTE radiation transfer for a six-level-with-continuum hydrogen atom and nine-level-with-continuum helium atom (the same atomic model solved by RADYN) with several background species treated in LTE as sources of background opacity. For each snapshot, the hydrogen atomic level populations from RADYN were used in RH and fixed so that RH did not iterate to the statistical equilibrium solution for hydrogen, as in Kerr et al. (2019a). This meant that nonequilibrium and nonthermal effects were included for hydrogen. This was done for (1) standard RH, (2) RH with coronal irradiation, and (3) RH with coronal irradiation and with nonthermal collisional ionization of helium. Comparing the resulting He I 10830 Å emission in each case demonstrated that photoionization via flare-enhanced He II 304 Å was not as important in comparison to coronal emission $\lambda < 504$ Å (similar to quiet Sun results of Wahlstrom & Carlsson (1994)) and He C_{nt}, from which we can conclude that omitting this in RADYN would not alter our overall conclusions.

3. He Ionization Stratification and Level Populations

Simulations that included He C_{nt} exhibited some important differences at early stages in the flare compared to those that did not. When He C_{nt} is present, some fraction of helium quickly becomes ionized to He II, even in the relatively cool chromosphere between $z \sim 1$ Mm and the TR. These locations were typically co-spatial with the peak of the electron-beam heating rate. Within fractions of a second, there can be as much as a ∼10%–20% He II fraction in the upper chromosphere, growing to an even larger fraction as the flare progresses and temperatures increase. In the absence of He C_{nt}, there are substantially fewer He II ions at those heights, and those only form later in the simulation when the chromospheric temperature has risen and coronal irradiance increased. As time progresses the differences between the two scenarios reduce, indicating that He C_{nt} play a dominant role only in the early phase of the flare and that later thermal processes and PRM increase in importance. In the weaker simulations, the smaller number of He C_{nt} results in a correspondingly smaller fraction of He II. In the stronger simulations, there is a larger fraction of He II, and the differences between including and omitting He C_{nt} reduce at a faster rate (presumably because the upper chromospheric temperature more rapidly increases). The same is true when a faster rate of flare energy injection is simulated.

Because the temperature is still too cool to fully ionize helium, there are recombinations of free electrons to He II → He I. These can take place to excited levels of helium, including the orthohelium states. Both $n_{\rm lower}$ and $n_{\rm upper}$ increase in population, with a strong peak in the mid-upper chromosphere, but with a wide tail to lower altitudes. Because

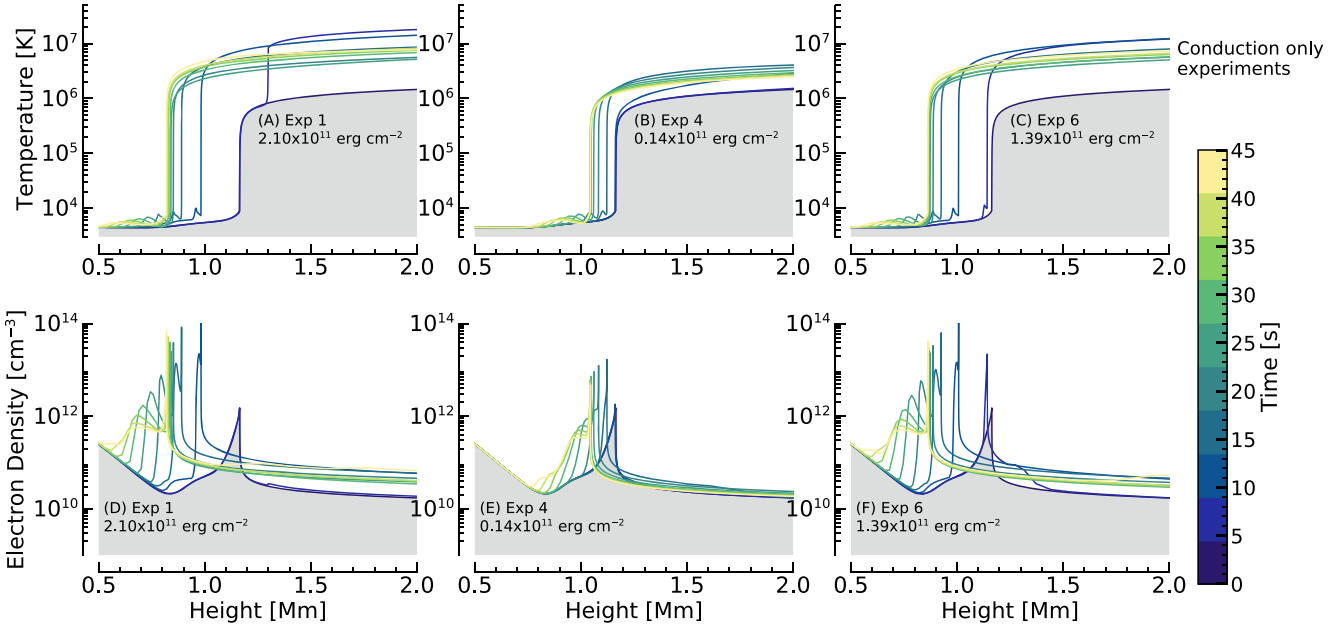

Figure 2. Temperature (top row) and electron density (bottom row) stratification as a function of time in the conduction-only flare simulations. Experiments 1, 4, and 6 are shown (total energy flux indicated). The grayscale shows the preflare stratification.

penetration depth scales with electron energy, simulations with a larger E_c exhibit a slightly deeper peak height and a larger vertical extent of enhanced orthohelium populations. Softer distributions more efficiently heat the upper chromosphere, so that thermal effects occur more quickly in weaker flares. Populations also scale with flare strength due to the larger number of ionizations.

These overpopulations of orthohelium would increase the opacity at $\lambda = 10830$ Å due to increased absorption of photospheric photons by the $^3S_1$ ($n_{\rm lower}$) level. Without He C_{nt}, there is no excess of recombinations through the excited levels at early times in the flare, and consequently, no initial increase in $\lambda = 10830$ Å opacity. Similar to the He ionization fraction, as the flare develops the populations of orthohelium in the two scenarios of with and without He C_{nt} become more similar, at least in the mid-upper chromosphere (height $z \sim [1–1.25]$ Mm). This happens faster in stronger flares and in flares with a softer spectrum (smaller E_c). This height range is where most of the nonthermal electron energy is deposited, and once the temperature has increased during the flare, thermal effects dominate the population of orthohelium at those altitudes. He C_{nt} clearly still play a dominant role at lower altitudes, and still act to populate orthohelium at $z \sim [1–1.25]$ Mm even though thermal processes drive the simulations with and without He C_{nt} closer. Generally, the magnitude and widths of the peaks of orthohelium population densities and He I fraction decrease with decreasing flare strength, and the time taken for the simulations with and without He C_{nt} to become similar decreases with increasing flare strength.

Inspecting Figures 3 and 4 clearly illustrates the differences that emerge in simulations with and without He C_{nt}, for a weak and stronger flare, respectively. In the lower energy simulation, while the peak of the populations are similar, the case with He C_{nt} clearly exhibits a tail that would increase the opacity of the He I 10830 line at these times. In the higher energy simulations, the mid-upper chromosphere contains a peak population of orthohelium that is extended over several hundred kilometers in simulations both with and without He C_{nt}. This is due to the strong chromospheric temperature in those simulations leading to thermal collisional ionization and recombination. Although they become similar rather quickly, there are a few seconds where the simulation with He C_{nt} has a larger orthohelium population than the simulation without He C_{nt}. See the Appendix for an example simulation with a smaller value of E_c.

It is, roughly speaking, the ratio of $n_{\rm upper}$ to $n_{\rm lower}$ that governs the intensity of the He I 10830 Å, and if the line is in absorption or emission. While both $n_{\rm upper}$ and $n_{\rm lower}$ increase during the flare, their ratio varies over time. Huang et al. (2020) showed that in their flare this ratio increased during their flare simulation at the time that the line went into strong emission. We demonstrate here how the behavior of this ratio changes over time in the scenario with and without He C_{nt}. This is shown in Figure 5, where we compare the ratios from three flare strengths with (top row) and without (bottom row) He C_{nt} (note the varying y-axis scale in each panel). This figure shows one of the harder nonthermal electron distributions ($E_c = 25$ keV) but the results are typical of all simulations.

In all flares with He C_{nt}, there is an initial decrease in the level population ratio, indicating that there is an increased amount of $n_{\rm lower}$ relative to $n_{\rm upper}$, compared to the preflare stratification, and therefore more absorptions. Stronger flares reverse this ratio quickly, eventually increasing significantly over the preflare. The line is in emission at these times. Flares with harder nonthermal electron distributions exhibit a stronger decrease, over a larger height range, for a longer period. See the Appendix for the $E_c = 15$ keV case.

At the locations where He I 10380 Å forms ($z \gtrsim 1$ Mm), this population ratio in the 1F10 simulations does not actually increase over the preflare value for the simulations with $E_c > 20$ keV. It does at lower altitudes, but because the line is optically thick during the flare, it is $z \gtrsim 1$ Mm that really matters. As we will show in the next section, the He I 10830 Å line did not go into emission in those experiments.

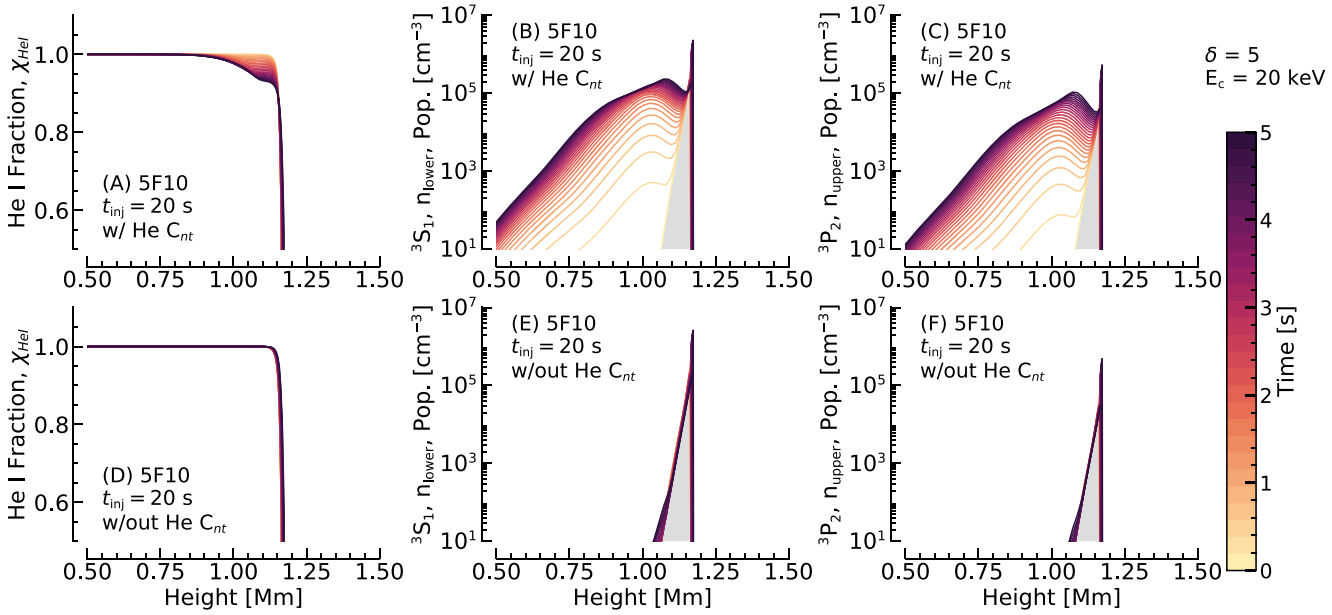

Figure 3. The He I fraction (A, D), and the population densities of the lower (B, E) and upper (C, F) levels of the He I 10830 Å line as a function of time in the initial stages of one of our flare simulations (5F10, $\delta = 5$, $E_c = 20$ keV, $\tau_{inj} = 20$ s). The top row is the case with He C_{nt} and the bottom row is the case without He C_{nt}.

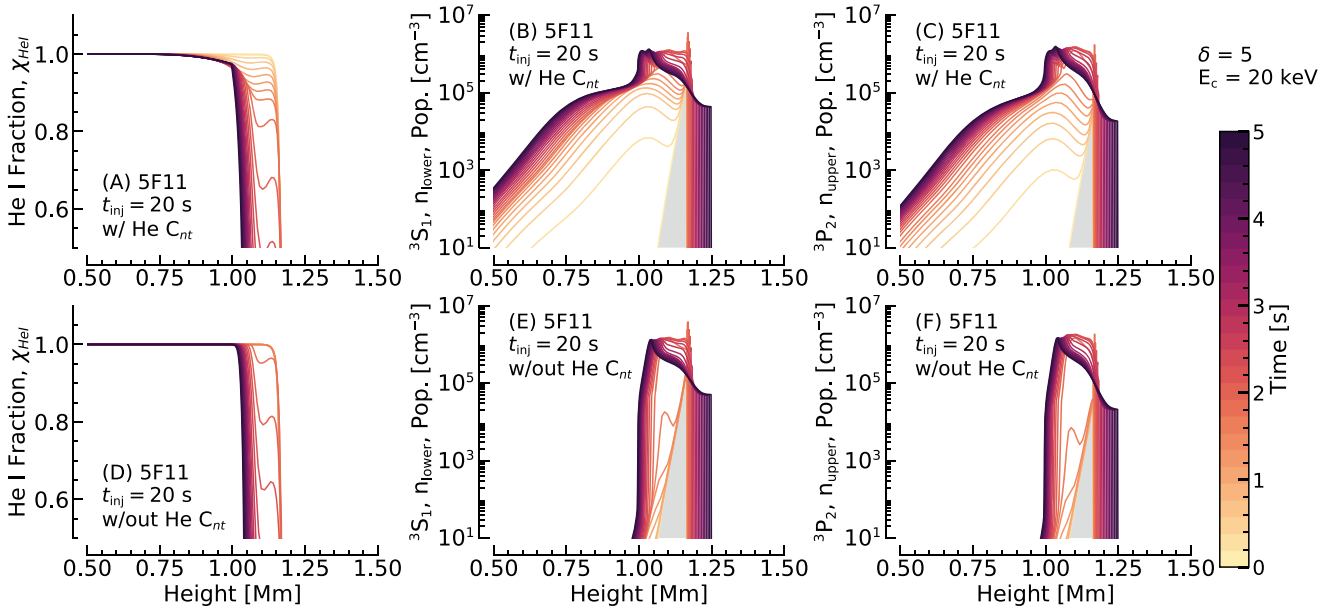

Figure 4. Same as Figure 3 but for a stronger flare (5F11, $\delta = 5$, $E_c = 20$ keV, $\tau_{inj} = 20$ s).

Omitting He C_{nt} results in the absence of this initial decrease in the ratio, with the ratio instead only increasing. Also, at times and in certain locations, the ratio in the scenario with He C_{nt} exceeds that of the scenario without He C_{nt}.

Now that we have determined that the inclusion or omission of He C_{nt} can result in notable differences to the stratification of the He I ionization fraction and orthohelium level population densities and that those properties are also dependent on flare strength and nonthermal electron distribution spectral hardness, we demonstrate how they are manifested in the emergent He I 10830 Å line intensity.

4. He I 10830 Å Response to Flares

4.1. Electron-beam-driven Flares

Every electron-beam-driven flare simulation that included He C_{nt} exhibited dimming in the initial phase of the flare, which is enhanced absorption over the preflare producing a negative contrast. With the exception of the weakest flares (1F10, $E_c > 20$ keV), the line subsequently went into emission, producing a positive contrast. Simulations that did not include He C_{nt} did not exhibit dimming during the heating phase—they only contained emission over the preflare.

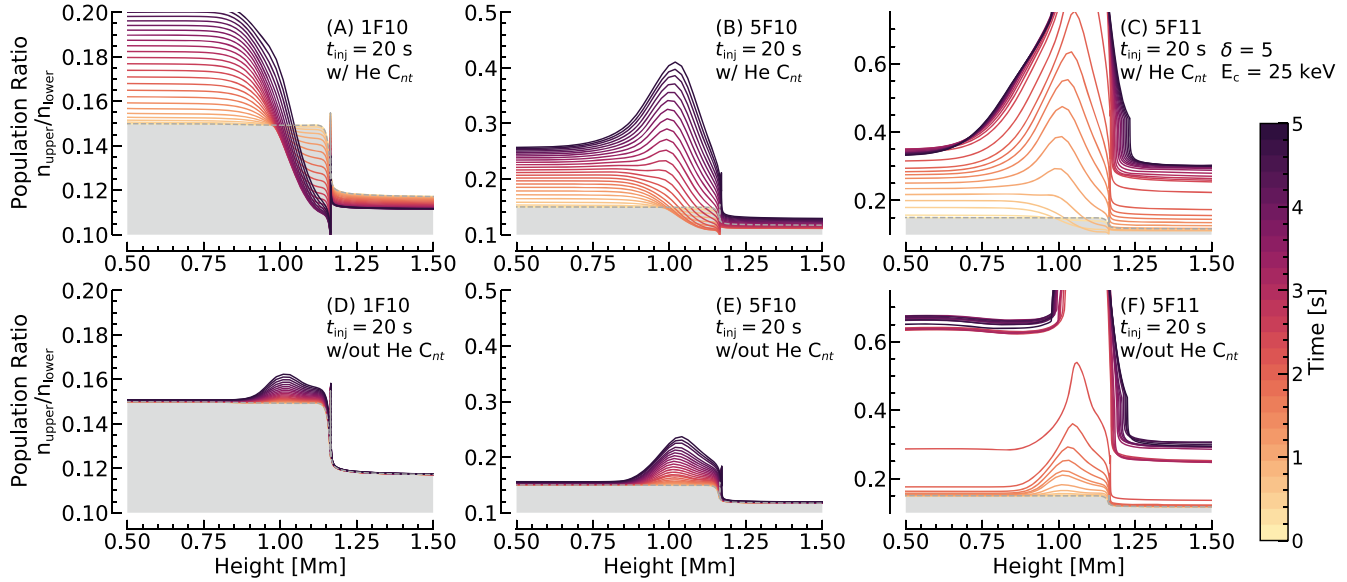

Figure 5. The ratio of the He I 10830 Å lines upper-to-lower level population densities in the initial stages of some flare simulations. The top row shows simulations with He C_{nt}, and the bottom row without He C_{nt}. Color represents time. In all experiments $\delta = 5$, $E_c = 25$ keV, and $\tau_{inj} = 20$ s. The total injected energy fluxes are 1×10 erg cm^{-2} (A, D), 5×10 erg cm^{-2} (B, E), and 5×11 erg cm^{-2} (C, F). The grayscale is the preflare.

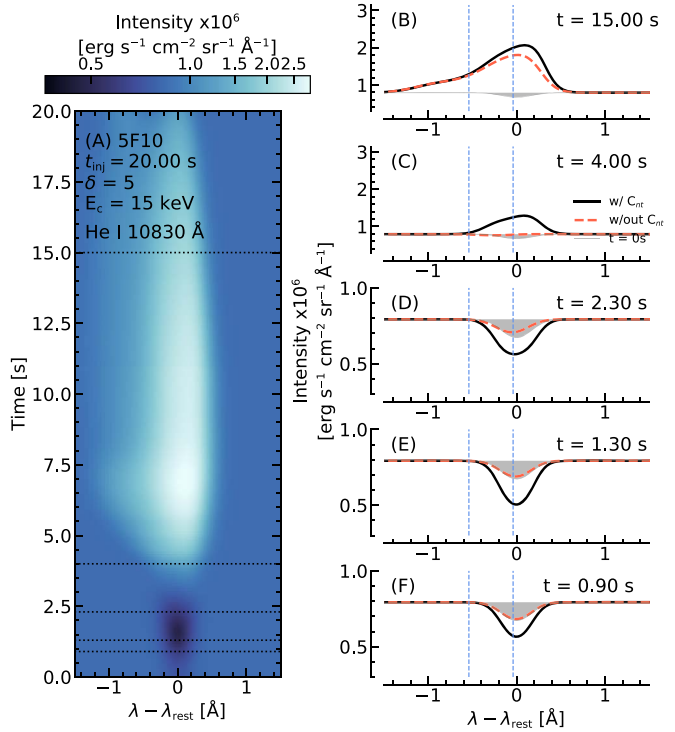

Figure 6. (A) The response of the He I 10830 Å line in a flare simulation (5F10, $\tau_{inj} = 20$ s, $E_c = 15$ keV, $\delta = 5$) where He C_{nt} are included. The dashed lines indicate the times shown in panels (B–F), which compares the simulation in panel A to the equivalent without He C_{nt}. In those panels, the black lines include helium nonthermal collisional ionization, and the red dashed lines do not. The gray dashed line is the $t = 0$ s profile. The dashed blue lines indicate the wavelength range imaged by Xu et al. (2016).

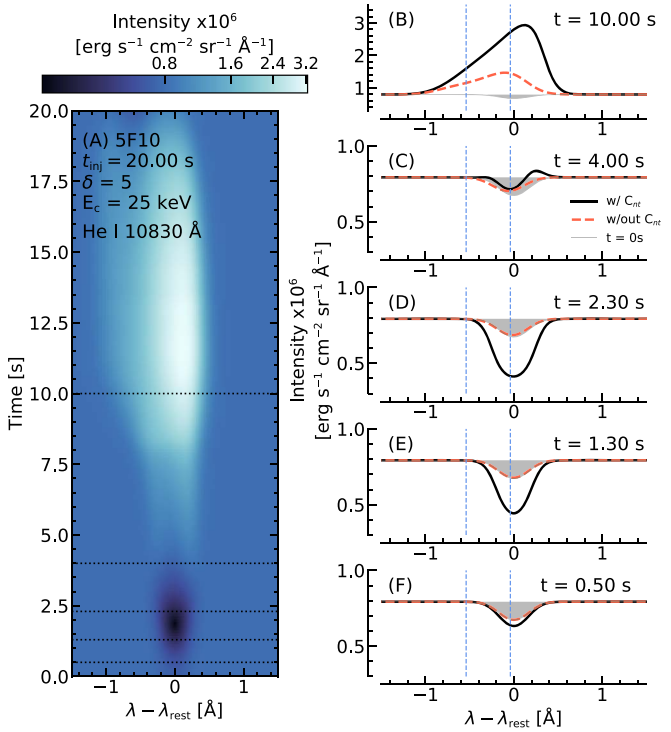

Figure 7. Same as Figure 6 but for a harder nonthermal electron distribution, with $E_c = 25$ keV.

Figures 6 and 7 show representative cases, the 5F10 $t_{inj} = 20$ s simulation with $E_c = 15$ keV and $E_c = 25$ keV, respectively. Panel (A) shows the line intensity (color) as a function of wavelength for the heating phase of the flare (color map scaled to the 2/5 power). The dark-colored patch at early times is the line dimming, which is a deeper absorption profile. After $t \sim 3$–4 s the line switches to being more intense than the preflare (though still in absorption, near the continuum level) before going strongly into emission a short time later. Both of these periods would be observed as a positive contrast. The line broadens, is Doppler shifted, and exhibits asymmetries. Though the line appears redshifted (the peak intensity is in the red wing), the line actually forms in upflowing plasma. Being optically thick, this results in the absorption profile shifting to the blue also, which preferentially absorbs blue-wing photons, giving rise to a red peak. This phenomenon has been

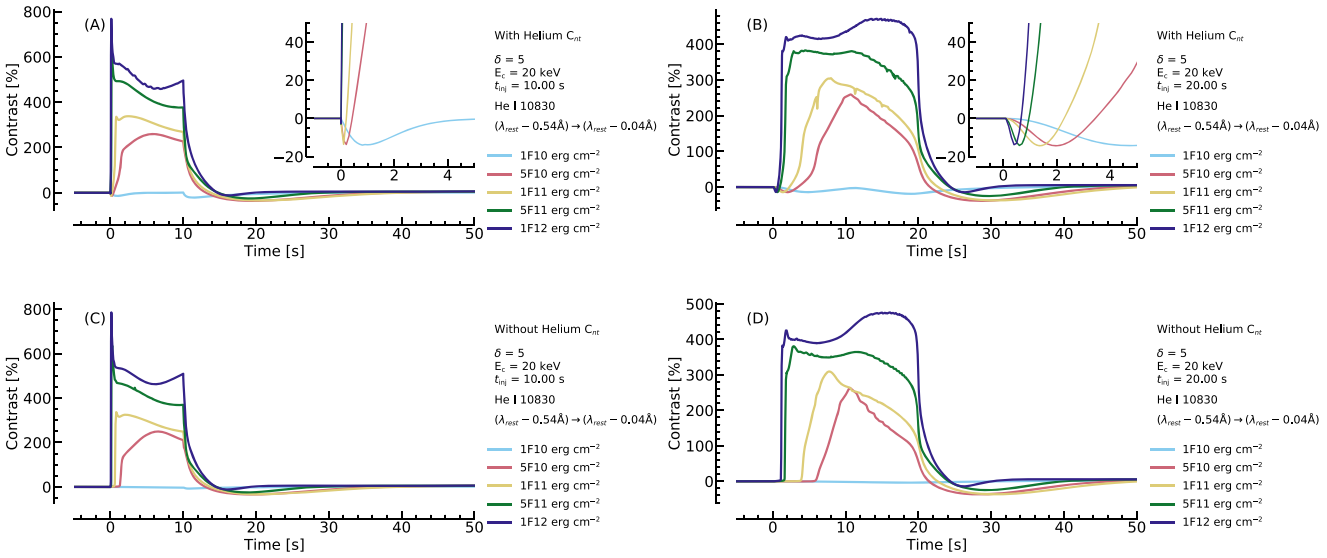

Figure 8. Lightcurves of the He I 10830 Å line, integrated over $\lambda_{\rm rest} - 0.54$ Å to $\lambda_{\rm rest} - 0.04$ Å. All simulations have $\delta = 5$, $E_c = 20$ keV, and the color represents total energy flux. Panels (A) and (B) are simulations including He C_{nt}, with $\tau_{\rm inj} = 10$ s and $\tau_{\rm inj} = 20$ s, respectively. Dimmings at flare-onset are present. Panels (C) and (D) show the simulation omitting He C_{nt} with $\tau_{\rm inj} = 10$ s and $\tau_{\rm inj} = 20$ s, respectively. Dimmings at flare onset are no longer present.

described in detail by, e.g., Kuridze et al. (2015, 2016) and Kerr et al. (2016) as concerns the Hα and Mg II h & k lines. Central reversal features are present in the line once it starts to go into emission. The duration and depth of the enhanced absorption feature both scale with increasing E_c.

Comparisons to the simulations without He C_{nt} are shown in panels (B–F) of each figure, which shows line profiles from five snapshots in the flare. Black lines are profiles including He C_{nt}, red dashed lines are those without He C_{nt}. The $t = 0$ s is also shown for context (gray shaded area). It is clear that He C_{nt} has a strong effect on the line. Not only is the dimming of the line absent when omitting He C_{nt}, but the overall intensity of the line is generally weaker, though by varying degrees throughout the duration of the flare.

Lightcurves of the integrated intensity show that the duration of the dimming varies strongly with flare strength and energy injection timescale. Weaker flares and flares with more gradual energy injection exhibit more sustained dimming. Some of the stronger flares, particularly those with $t_{\rm inj} = 10$ s, have dimmings that last only fractions of a second (unobservable with current instrumentation). Flares that include He C_{nt} generally have stronger total emission than those without. The variation of dimmings as a function of total flare energy and injection timescale is shown in Figure 8. Shown in that figure are lightcurves (presented as contrasts over the preflare, $C = (I_{\rm flare} - I_{t=0})/I_{t\ =\ 0} \times 100$) from flares with $E_c = 20$ keV, for the range of flare energies simulated. Panel (A) shows $\tau_{\rm inj} = 10$ s, and panel (B) shows $\tau_{\rm inj} = 20$ s. The latter case contains more sustained enhanced absorption. Panels (C) and (D) show the same but with He C_{nt} omitted, where no enhanced absorption is present. In that figure, the intensity was integrated over $\lambda_{\rm rest} - 0.54$ Å to $\lambda_{\rm rest} - 0.04$ Å, the same passband as the BBSO observations reported by Xu et al. (2016). Mass flows do Doppler shift the line and lead to asymmetries, so the choice of passband will affect the lightcurve but did not artificially produce or remove the enhanced absorption feature. Integrating over a passband centered on the line core gave qualitatively similar results, but of course with somewhat different numerical values.

As well as varying with flare strength, both the strength and duration of the absorption feature vary as a function of spectral hardness of the nonthermal electron distribution. A larger E_c produced deeper, more sustained absorptions. Figure 9 illustrates for a fixed energy flux 1F11 $\tau_{\rm inj} = 20$ s the effect of varying the low-energy cutoff. See also Section 5.

The weakest set of flares in our study, the 1F10 simulations, stays in absorption for the entirety of the heating phase when He C_{nt} is included, apart from the softest distributions $E_c = [10, 15]$ keV, presumably because in those simulations the upper chromosphere became hot enough to drive thermal collisions later in the flare. In the harder simulations, the temperature rise would have been more modest and not enough to combat the greater increase in opacity present because a larger swathe of the chromosphere produced additional orthohelium. Interestingly, if He C_{nt} were omitted, then these weakest simulations do go into emission, likely because there is no additional opacity to overcome so that even modest temperature enhancements can increase He I 10830 Å emission.

While we can qualitatively match observations in the sense that a period of enhanced absorption is produced at flare onset, and while we obtain negative contrasts similar to those recently observed by Xu et al. (2016), our simulations predict a substantially shorter period of dimming than observed and a larger positive contrast when the line is in emission. Our modeling predicts only several seconds of dimming, compared to several tens to more than 100 s of dimming in the observations of Xu et al. (2016). A follow-up to this work will focus on the formation properties of the line and attempt to identify reasons behind this discrepancy. For now, we note that the only way that we have thus far been able to extend the period of enhanced absorption was to initially inject a very weak beam before ramping up the energy flux to what we generally consider to be standard flare values. If we inject a beam with $\delta = 5$, $E_c = 25$ keV, and instantaneous energy flux $F_{\rm ins} = 5 \times 10^8$ erg cm^{-2} s^{-1} for a period of 30 s before increasing the energy flux to $F_{\rm ins} = 1 \times 10^9$ erg cm^{-2} s^{-1} for 5 s, then to $F_{\rm ins} = 5 \times 10^9$ erg cm^{-2} s^{-1} for 5 s, and finally to $F_{\rm ins} = 5 \times 10^{10}$ erg cm^{-2} s^{-1} for 10 s, then we obtain the

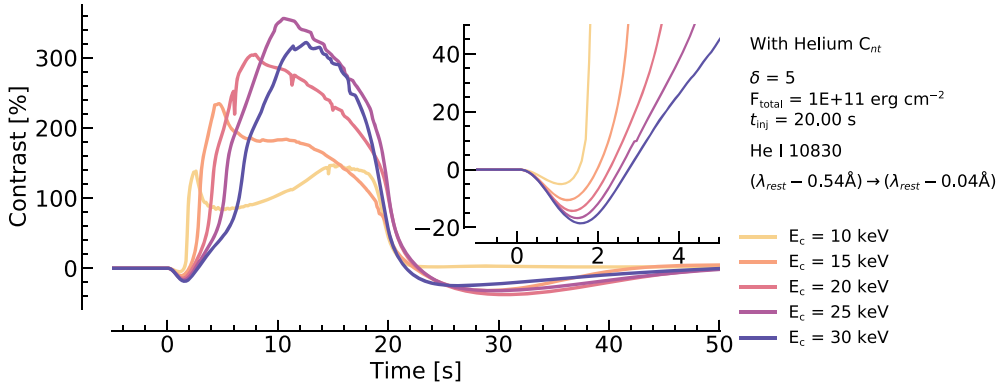

Figure 9. Lightcurves of He I 10830 Å for simulations with $\delta = 5$, total energy flux 1F11, $\tau_{inj} = 20$ s, and a range of low-energy cutoff values $E_c = [10, 15, 20, 25, 30]$ keV. He C_{nt} are included.

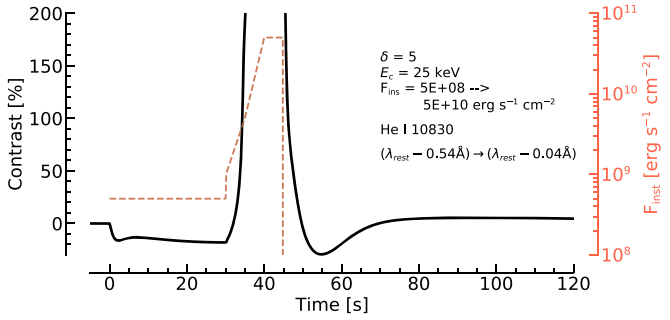

Figure 10. Lightcurve of He I 10830 Å for the simulation with $\delta = 5$, $E_c = 25$ keV, which initially had a weak energy flux of 5×10^8 erg cm^{-2} s^{-1} before ramping up to 5×10^{10} erg cm^{-2} s^{-1}. He C_{nt} are included. The injected instantaneous energy flux is shown as the red dashed line for reference. To focus on the initial dimming, the contrast scale has been clipped.

lightcurve shown in Figure 10. The enhanced absorption is present for the duration of the weak beam heating, and only when the energy flux increases, and the chromospheric temperature rises, does the line go into emission. The time profile of the energy flux is shown on the right-hand axis of Figure 10 for reference.

4.2. Flares Driven by Thermal Conduction

It has been established that in electron-beam-driven flares, the CRM dominates over PRM in overpopulating orthohelium in the initial stages, leading to enhanced absorption. The role of the PRM in the later stages of the flare will be explored in more detail in a follow-up work, but it seems that it takes some time for coronal irradiance to increase sufficiently drive additional photoionization of helium. By the time the corona has been heated and mass loaded, the temperature in the chromosphere is high enough that the line is in emission.

A reasonable question is then, can direct heating of the corona before the chromosphere is heated increase irradiance and photoionizations of helium and lead to enhanced absorption? Direct in situ heating of plasma at loop tops has been suggested as necessary to explain certain flare observations (e.g., Battaglia et al. 2009; Holman 2016; Warmuth & Mann 2020, and references therein), and recent simulation results suggest that energy release from reconnection (Cheung et al. 2019) and retraction of flare loops (Longcope & Klimchuk 2015; Longcope et al. 2016, 2018) can deposit

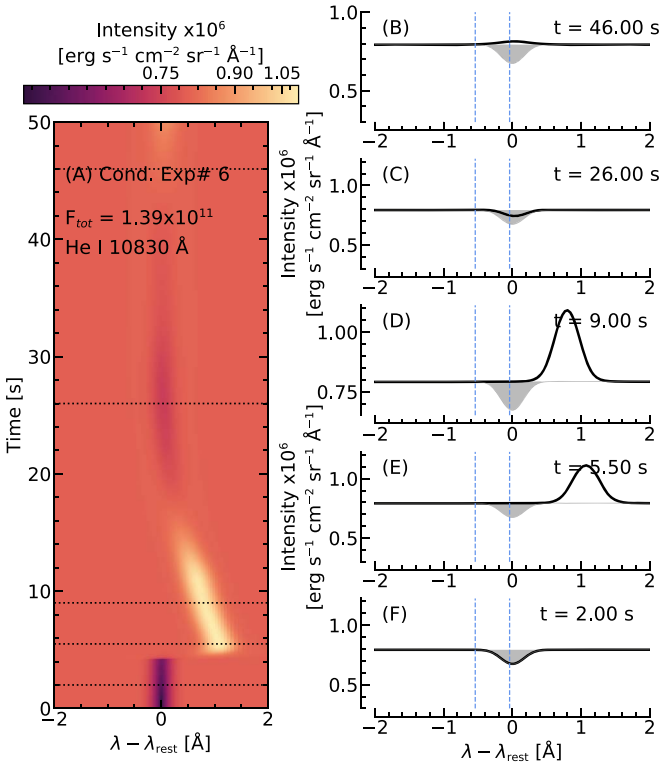

Figure 11. Same as Figure 6 but for direct heating experiment #6.

energy at the loop tops. This energy would then be transported to the lower atmosphere via the conductive flux.

We modeled purely thermal flares, depositing energy directly into the corona. In those experiments, the coronal temperature increase preceded the chromospheric temperature increase. However, even in this circumstance, there was an insufficient increase in coronal irradiation to produce an overpopulation of orthohelium and therefore enhanced absorption. Figure 11 shows the He I 10830 Å line profile evolution for one of our conduction experiments, and Figure 12 shows the temporal evolution of the contrast for all seven experiments. No initial period of enhanced absorption is present.

This is likely because while the coronal temperature increased early in the flare, the coronal density did not increase until ablation of chromospheric plasma began to mass load the loop. The coronal radiation field would scale strongly with the

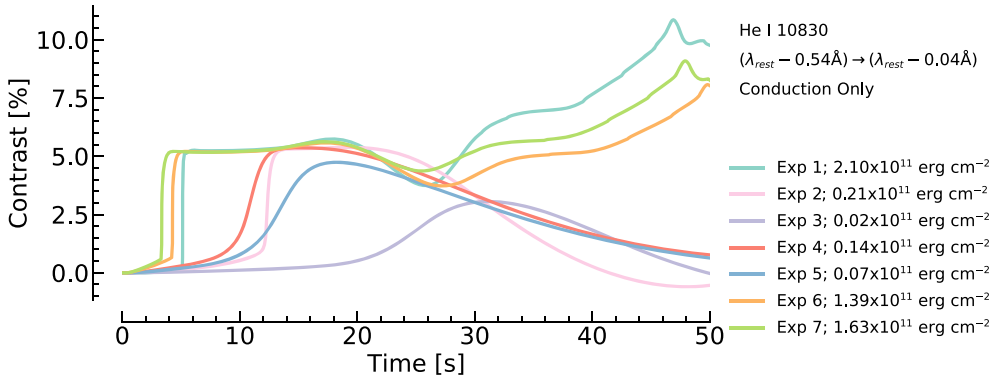

Figure 12. Lightcurves of He I 10830 Å for simulations driven by in situ coronal heating and thermal conduction only. Wavelength is integrated over $\lambda_{\rm rest} - 0.54$ Å to $\lambda_{\rm rest} - 0.04$ Å.

emission measure of the plasma. By the time this happens, the chromosphere has began to be heated.

These simulations suggest that flares with little or no nonthermal hard X-ray emission would be unlikely to exhibit enhanced absorption of orthohelium lines. Observations of enhanced absorption early in the flare before mass flows are generated are therefore indicative of the presence of the accelerated particles.

5. Properties of Absorption Feature

In the preceding sections, we have demonstrated that enhanced absorption of He I 10830 Å takes place when nonthermal collisional ionizations of helium are present and that the duration of the absorption varies with flare strength and spectral distribution of the impacting nonthermal electron distribution. Here we discuss how properties of the absorption line can be related to the properties of the nonthermal electron distribution.

The equivalent width, $W_{\rm eq}$, gives a measure of the strength of the absorption line:

$$W_{\rm eq} = \int \frac{I_c - I_\lambda}{I_c} d\lambda, \tag{2}$$

where I_c is the intensity of the continuum and I_λ is the intensity at wavelength λ. The maximum value of $W_{\rm eq}$ in each simulated flare, $W_{\rm eq,max}$, was used to define the maximum strength of enhanced absorption for that flare. As a measure of the duration of absorption, we find the time taken for the line to go into emission, $t_{\rm emiss}$, as the time at which $W_{\rm eq}$ becomes negative (because in our definition of Equation (2) an emission line returns a negative value). Figure 13 shows a scatter plot of $W_{\rm eq,max}$ as a function of $t_{\rm emiss}$. The symbol size is scaled to represent increasing E_c, and the symbol color represents the total injected energy flux. Circles are flares with $\tau_{\rm inj} = 10$ s, and crosses are $\tau_{\rm inj} = 20$ s. In that figure, some of the weakest flares (green symbols) are not present as they never go into emission. There is a cluster of simulations that show small $W_{\rm eq,max}$ and very short $t_{\rm emiss}$. Those are the strongest flares. Of those with longer duration periods of absorption, for a fixed flare strength, a larger E_c results in a larger $t_{\rm emiss}$, and a larger $W_{\rm eq,max}$. Decreasing flare strength lengthens the period of absorption, giving a larger $t_{\rm emiss}$. Flares with a more gradual energy injection timescales have longer duration period of absorption.

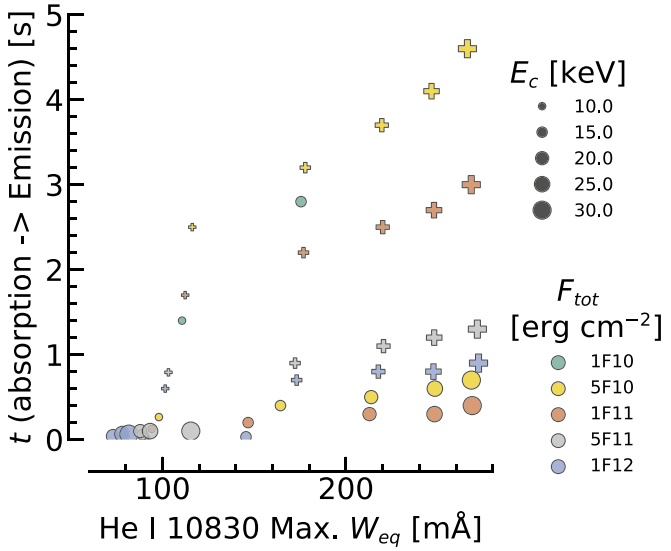

Figure 13. The relationship between absorption properties and nonthermal electron distribution. The maximum equivalent width of the absorption profile in each simulation is shown against the time taken for the line to go into emission. Colors refer to flare strength (total injected energy flux) and symbol size the low-energy cutoff E_c. Circles are those simulations with $\tau_{\rm inj} = 10$ s, and crosses are those with $\tau_{\rm inj} = 20$ s.

While the magnitude of absorption depends quite strongly on E_c, it does not really show a strong relationship to flare strength.

Exploring the seeming lack of relationship between $W_{\rm eq}$ and flare strength further, we show in Figure 14 $W_{\rm eq,max}$ as a function of the instantaneous injected energy flux (erg s^{-1} cm^{-2}) at the time of maximum $W_{\rm eq,max}$ (panel A) and as a function of the total energy flux injected between $t = 0$ s and time of maximum $W_{\rm eq,max}$. Color is the low-energy cutoff. The former (panel A) shows us the strength of the bombarding electron flux at the time when $W_{\rm eq}$ is largest, and the latter shows us the cumulative amount of energy deposited during the flare up to the point that $W_{\rm eq}$ is largest. There is little relation between the energy flux and the strength of the absorption feature. The dependence on E_c is again very clear, however. The clusters in the top left of panel (A) and bottom left of panel (B) are the strongest flares with $\tau_{\rm inj} = 10$ s. Future work will investigate this further, determining if the number flux of electrons in certain energy ranges can produce a clearer relationship.

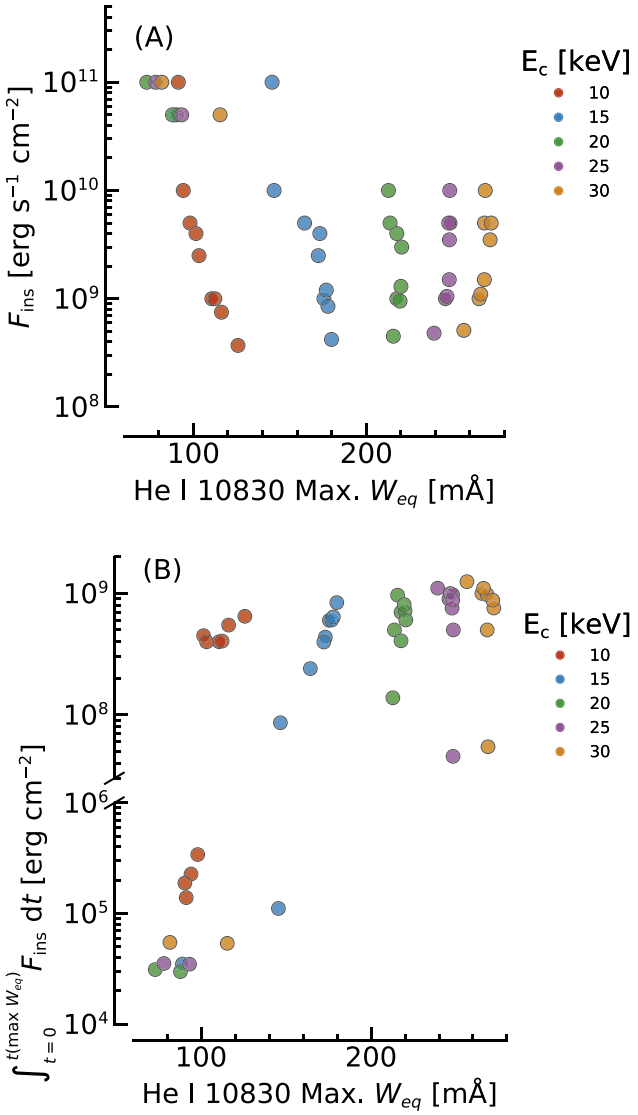

Figure 14. The maximum equivalent width of the He I 10830 Å line, $W_{eq,max}$, as a function of (A) instantaneous injected energy flux at that time, and (B) the injected energy flux integrated from $t = 0$ to the time of $W_{eq,max}$. Color is low-energy cutoff E_c.

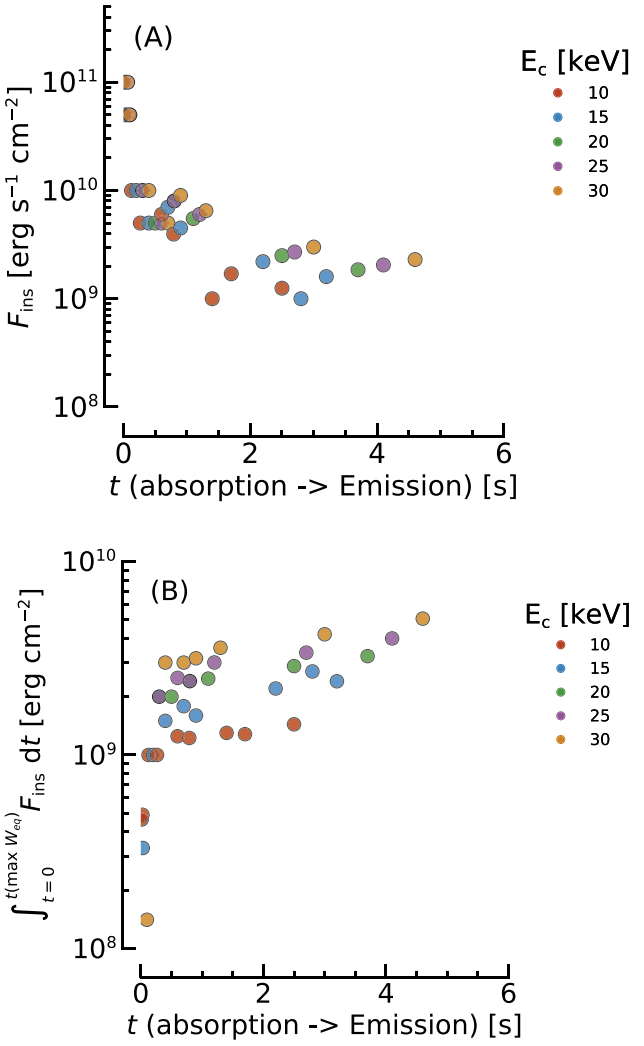

Figure 15. The time taken for He I 10830 Å to reach emission, t_{emiss}, as a function of (A) instantaneous injected energy flux at that time, and (B) the injected energy flux integrated from $t = 0$ to t_{emiss}. Color is the low-energy cutoff E_c.

In Figure 15, we show t_{emiss} as a function of the instantaneous injected energy flux (erg s^{-1} cm^{-2}) at t_{emiss} (panel A) and as a function of the total energy flux injected between $t = 0$ s and t_{emiss}. Color is again the low-energy cutoff. Here it seems that the smaller the instantaneous flux, the longer the period of absorption. Note that in that figure, the $\tau_{inj} = 10$ s simulations result in the horizontal groupings (because those simulations have a constant F_{ins}). Panel (B) shows that a longer period of absorption implies a larger total injected flux, for a fixed E_c.

Taking all of this information together, we have the following picture: (1) flares with harder E_c penetrate more deeply, producing orthohelium over a wider vertical extent, thus building up greater opacity. (2) The absorption of He I 10830 Å photons is increased, giving a deeper, wider absorption profile. These harder nonthermal electron distributions heat the upper atmosphere less efficiently than softer distributions, so that more time is allowed to pass (and energy flux be deposited) before the upper chromosphere temperature and electron density reach the threshold for thermal processes drive the line into emission. (3) Increasing the flare strength means these thresholds are reached sooner, as does increasing the rate of energy deposition. This picture of chromospheric temperature driving the line into emission is consistent with simulations that only include thermal collisional ionization and recombination as a pathway to populate orthohelium. Schmidt et al. (2012) modeled stellar flares using the RH code, but without including He C_{nt} or coronal irradiation, finding that the line did go into emission without the inclusion of CRM or PRM, but that it was weaker than observed (the ratio of He I 10830 Å to other infrared lines was too small). So, without the CRM and PRM, the line does go into emission when the temperature increases, but those two mechanisms increase the line intensity.

6. Summary and Conclusions

Using the radiation hydrodynamics code RADYN, we performed a large parameter study of electron-beam-driven solar flares, covering a variety of flare strengths and low-energy cutoffs. From that grid of simulations, we analyzed the

behavior of the He I 10830 Å line, with a particular focus on the early phase which has been observed to undergo a period of enhanced absorption—a so-called negative flare. We found that:

1. To produce enhanced absorption features of He I 10830 Å, it is necessary for nonthermal collisional ionization of helium to be present. Experiments that omit He C_{nt} resulted exclusively in emission, as did simulations of flares driven only by thermal conduction;
2. In most of our flare simulations, He I 10830 Å went into emission, but the weakest flares in our sample did not, despite including He C_{nt}. Therefore, observations, such as those by Kobanov et al. (2018)m of weak flares that exhibit absorption for the duration, are still compatible with the nonthermal collisional ionization–recombination mechanism.
3. The duration of the emission is a function of both the flare strength and the hardness of the beam (here explored through the low-energy cutoff E_c). Strong flares exhibit a vanishingly short period of enhanced absorption. Enhanced absorption persists longer in weaker flares. Increasing E_c results in longer duration enhanced absorption. Together, these point to the fact that stronger and softer beams heat the upper atmosphere, more quickly producing conditions favorable to drive He I 10830 Å into emission.
4. The strength of the absorption feature scales with the low-energy cutoff. This can be understood as a larger swathe of the chromosphere undergoing a higher rate of nonthermal collisional ionizations, increasing the opacity at 10830 Å and absorbing more photospheric radiation.
5. We were unable to match the observed duration of enhanced absorption, with our simulations predicting only a few seconds compared to the observed several tens to hundreds of seconds. Injecting an electron beam with very low-energy flux for 30 s before ramping up the energy flux to a more typical level did produce an extended period of absorption that persisted as long as the weak beam was bombarding the chromosphere. This may indicate that a weak flux of nonthermal particles is present in the mid-upper chromosphere before the bulk of flare energy is deposited into each source. Follow-up work will also investigate different temporal properties of energy injection, such as a series of very short pulses or multithreaded modeling (e.g., Reep et al. 2018).

Our results demonstrate that, at least in the early phase of the flare, nonthermal collisional ionizations dominate the formation of orthohelium. In a forthcoming paper, we will elucidate the formation properties of orthohelium in more detail, investigating if nonthermal collisions dominate only in the early phase or throughout the flare duration. That work will also discuss more comprehensively the conditions necessary to bring the line into emission. This latter point is important to both understand the plasma properties that we observe, but also to be able to resolve the discrepancy with regard to the shorter-than-observed duration of enhanced absorption.

That these He I 10830 Å dimmings occur after the initial deposition of flare energy into the chromosphere, having been observed to be present at the narrow leading edge of flare ribbons, is particularly interesting given other recent work regarding the early phases of flare sources. Panos et al. (2018) analyzed Interface Region Imaging Spectrograph (IRIS; De Pontieu et al. 2014) Mg II h & k spectroscopic observations of the leading edge of flare ribbons, finding that unique profiles were present. These profiles were extremely broad and double peaked, with blueshifted central reversals, differing from the single-peaked profiles typically associated with flare ribbons. Also using IRIS, Jeffrey et al. (2018) studied a small flare (B class) with a very high cadence of 1.7 s. They found that the increase and peak of the nonthermal line width of the Si IV 1402.77 Å line preceded the rise and peak of line intensity. This was interpreted as a sign that MHD turbulence was present in flare footpoints before the plasma was strongly heated and that this turbulence likely contributed to the heating. Our simulation results also hint that nonthermal processes may be occurring for some time before the chromospheric temperature increases significantly (conclusion #4). Observations of the leading edge of flare ribbons with a subsecond-to-second cadence, and high spectral and spatial resolution, should be made to shed light on nonthermal processes and energy transport in solar flares.

Observations of orthohelium have the potential to act as a diagnostic of energy input via nonthermal particle precipitation during solar flares, particularly weaker events. Future modeling efforts must aim to determine to what extent we can exploit such observations, including modeling the He I D3 lines in solar flares. Liu et al. (2013) observed a flare in which He I D3 was undergoing enhanced absorption, while the He I 10830 Å line was already in emission. Differences in the formation and response in flares from these lines that share energy levels are likely a fruitful route to diagnostics of flare energy transport. We have already begun the process of including the He I D3 lines in our simulations. Spectroscopic observations are important to obtain a more comprehensive understanding of the response of the lines during flares and to better interrogate the models. These will be available via the Daniel K. Inouye Solar Telescope (DKIST), BBSO/GST, and the Swedish Solar Telescope (SST) during the current solar cycle. Further, while we have discussed only electron beams as a source of nonthermal particles that drive nonthermal collisional ionization, there has been speculation regarding the role of Alfvénic waves in flares, including their ability to locally accelerate particles in the chromosphere (e.g., Fletcher & Hudson 2008). The rate of nonthermal collisions that would result from such a distribution of electrons should be explored and compared to the electron-beam case.

G.S.K., Y.X., V.P., and H.W. acknowledge financial support from the NASA ROSES Heliophysics Supporting Research program (grant# NASA 80NSSC19K0859). J.C.A. acknowledges funding from NASA's Heliophysics Innovation Fund and NASA's Heliophysics Supporting Research program. V.S. acknowledges financial support from an NSF FDSS grant. We acknowledge NSF grant ATM-1954737. We thank the referee for comments that improved the clarity of our manuscript.

Appendix
Comparing Different Experimental Set-ups

Figure 16 shows the He ionistion fraction and orthohelium populations for a simulation with $E_c = 15$ keV (compare to Figure 3). Figure 17 shows the population ratios for simulations with $E_c = 15$ keV (compare to Figure 5).

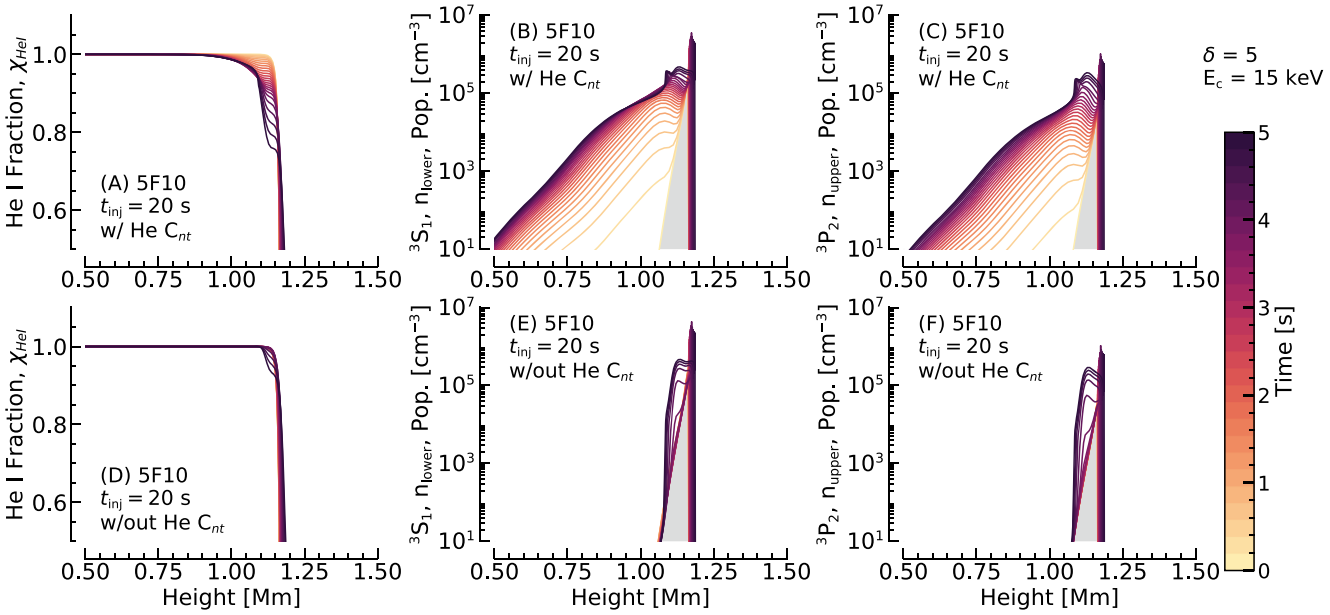

Figure 16. Same as Figure 3 but for a softer nonthermal electron distribution, with $E_c = 15$ keV.

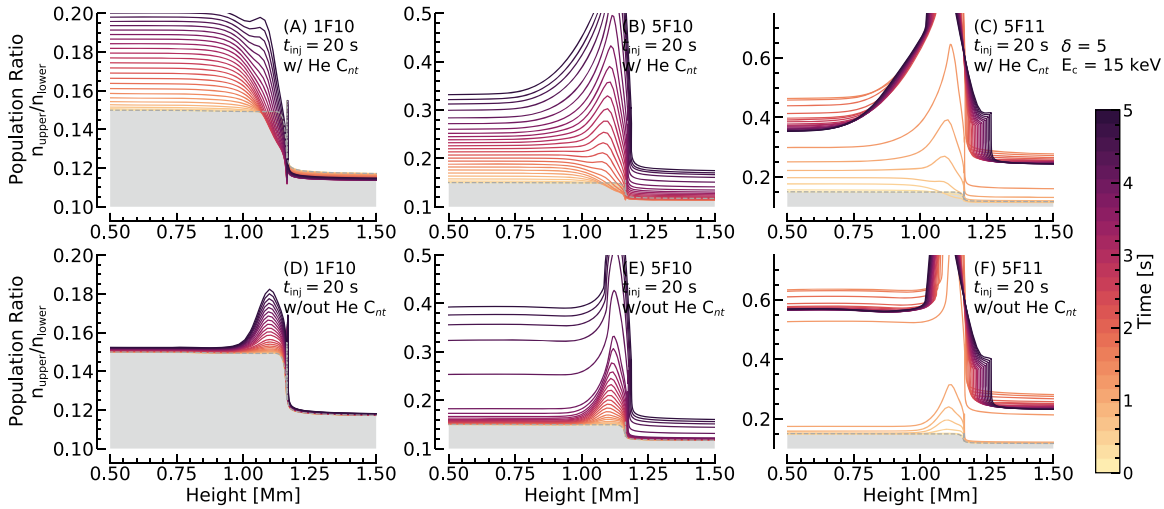

Figure 17. Same as Figure 5 but for a softer nonthermal electron distribution, with $E_c = 15$ keV

ORCID iDs

Graham S. Kerr https://orcid.org/0000-0001-5316-914X
Joel C. Allred https://orcid.org/0000-0003-4227-6809
Vanessa Polito https://orcid.org/0000-0002-4980-7126
Viacheslav M. Sadykov https://orcid.org/0000-0002-4001-1295
Nengyi Huang https://orcid.org/0000-0001-9049-0653
Haimin Wang https://orcid.org/0000-0002-5233-565X

References

Abbett, W. P., & Hawley, S. L. 1999, ApJ, 521, 906
Aboudarham, J., & Henoux, J. C. 1986, A&A, 168, 301
Allred, J. C., Alaoui, M., Kowalski, A. F., & Kerr, G. S. 2020, ApJ, 902, 16
Allred, J. C., Hawley, S. L., Abbett, W. P., & Carlsson, M. 2005, ApJ, 630, 573
Allred, J. C., Kowalski, A. F., & Carlsson, M. 2015, ApJ, 809, 104
Andretta, V., & Jones, H. P. 1997, ApJ, 489, 375
Arnaud, M., & Rothenflug, R. 1985, A&AS, 60, 425
Avrett, E. H., Fontenla, J. M., & Loeser, R. 1994, in Infrared Solar Physics, ed. D. M. Rabin, J. T. Jefferies, & C. Lindsey, 154 (Dordrecht: Kluwer Academic Publishers), 35
Battaglia, M., Fletcher, L., & Benz, A. O. 2009, A&A, 498, 891
Brown, S. A., Fletcher, L., Kerr, G. S., et al. 2018, ApJ, 862, 59
Cao, W., Gorceix, N., Coulter, R., et al. 2010, AN, 331, 636
Carlsson, M., & Stein, R. F. 1992, ApJL, 397, L59
Carlsson, M., & Stein, R. F. 1995, ApJL, 440, L29
Carlsson, M., & Stein, R. F. 1997, ApJL, 481, 500
Centeno, R., Trujillo Bueno, J., Uitenbroek, H., & Collados, M. 2008, ApJ, 677, 742
Cheung, M. C. M., Rempel, M., Chintzoglou, G., et al. 2019, NatAs, 3, 160
De Pontieu, B., Title, A. M., Lemen, J. R., et al. 2014, SoPh, 289, 2733
Dere, K. P., Landi, E., Mason, H. E., Monsignori Fossi, B. C., & Young, P. R. 1997, A&AS, 125, 149
Ding, M. D., Li, H., & Fang, C. 2005, A&A, 432, 699
Ding, M. D., Liu, Y., Yeh, C. T., & Li, J. P. 2003, A&A, 403, 1151
Dorfi, E. A., & Drury, L. O. 1987, JCoPh, 69, 175
Du, Q.-S., & Li, H. 2008, ChJAA, 8, 723
Fang, C., Henoux, J. C., & Gan, W. Q. 1993, A&A, 274, 917
Fletcher, L., & Hudson, H. S. 2008, ApJ, 675, 1645
Fuhrmeister, B., Czesla, S., Hildebrandt, L., et al. 2020, A&A, 640, A52

Goldberg, L. 1939, ApJ, 89, 673
Golding, T. P., Carlsson, M., & Leenaarts, J. 2014, ApJ, 784, 30
Golding, T. P., Leenaarts, J., & Carlsson, M. 2016, ApJ, 817, 125
Goode, P. R., & Cao, W. 2012, in ASP Conf. Ser., 463, Second ATST-EAST Meeting: Magnetic Fields from the Photosphere to the Corona, ed. T. R. Rimmele et al. (San Francisco, CA: ASP), 357
Graham, D. R., Cauzzi, G., Zangrilli, L., et al. 2020, ApJ, 895, 6
Harvey, K. L., & Recely, F. 1984, SoPh, 91, 127
Henoux, J. C., Aboudarham, J., Brown, J. C., van den Oord, G. H. J., & van Driel-Gesztelyi, L. 1990, A&A, 233, 577
Holman, G. D. 2016, JGRA, 121, 667
Holman, G. D., Aschwanden, M. J., Aurass, H., et al. 2011, SSRv, 159, 107
Huang, N., Sadykov, V. M., Xu, Y., Jing, J., & Wang, H. 2020, ApJL, 897, L6
Jeffrey, N. L. S., Fletcher, L., Labrosse, N., & Simões, P. J. A. 2018, SciA, 4, eaav2794
Kašparová, J., Varady, M., Heinzel, P., Karlický, M., & Moravec, Z. 2009, A&A, 499, 923
Kerr, G. S., Allred, J. C., & Carlsson, M. 2019a, ApJ, 883, 57
Kerr, G. S., Allred, J. C., & Polito, V. 2020, ApJ, 900, 18
Kerr, G. S., Carlsson, M., Allred, J. C., Young, P. R., & Daw, A. N. 2019b, ApJ, 871, 23
Kerr, G. S., Fletcher, L., Russell, A. J. B., & Allred, J. C. 2016, ApJ, 827, 101
Kobanov, N., Chelpanov, A., & Pulyaev, V. 2018, JASTP, 173, 50
Kowalski, A. F., Allred, J. C., Daw, A., Cauzzi, G., & Carlsson, M. 2017, ApJ, 836, 12
Kowalski, A. F., Hawley, S. L., Carlsson, M., et al. 2015, SoPh, 290, 3487
Kuridze, D., Mathioudakis, M., Christian, D. J., et al. 2016, ApJ, 832, 147
Kuridze, D., Mathioudakis, M., Simões, P. J. A., et al. 2015, ApJ, 813, 125
Landi, E., Young, P. R., Dere, K. P., Del Zanna, G., & Mason, H. E. 2013, ApJ, 763, 86
Leenaarts, J., Golding, T., Carlsson, M., Libbrecht, T., & Joshi, J. 2016, A&A, 594, A104
Li, H., You, J., & Du, Q. 2006, SoPh, 235, 107
Li, H., You, J., Yu, X., & Du, Q. 2007, SoPh, 241, 301
Libbrecht, T., Bjørgen, J. P., Leenaarts, J., et al. 2020, arXiv:2010.15946
Libbrecht, T., de la Cruz Rodríguez, J., Danilovic, S., Leenaarts, J., & Pazira, H. 2019, A&A, 621, A35
Liu, C., Xu, Y., Deng, N., et al. 2013, ApJ, 774, 60
Longcope, D., Qiu, J., & Brewer, J. 2016, ApJ, 833, 211
Longcope, D., Unverferth, J., Klein, C., McCarthy, M., & Priest, E. 2018, ApJ, 868, 148
Longcope, D. W., & Klimchuk, J. A. 2015, ApJ, 813, 131
Machado, M. E., Avrett, E. H., Vernazza, J. E., & Noyes, R. W. 1980, ApJ, 242, 336
Panos, B., Kleint, L., Huwyler, C., et al. 2018, ApJ, 861, 62
Penn, M. J. 2000, SoPh, 197, 313
Penn, M. J., & Kuhn, J. R. 1995, ApJL, 441, L51
Polito, V., Testa, P., Allred, J., et al. 2018, ApJ, 856, 178
Polito, V., Testa, P., & De Pontieu, B. 2019, ApJL, 879, L17
Reep, J. W., Polito, V., Warren, H. P., & Crump, N. A. 2018, ApJ, 856, 149
Rubio da Costa, F., & Kleint, L. 2017, ApJ, 842, 82
Rubio da Costa, F., Kleint, L., Petrosian, V., Liu, W., & Allred, J. C. 2016, ApJ, 827, 38
Schmidt, S. J., Kowalski, A. F., Hawley, S. L., et al. 2012, ApJ, 745, 14
Simões, P. J. A., Kerr, G. S., Fletcher, L., et al. 2017, A&A, 605, A125
Uitenbroek, H. 2001, ApJ, 557, 389
van Driel-Gesztelyi, L., Hudson, H. S., Anwar, B., & Hiei, E. 1994, SoPh, 152, 145
Vernazza, J. E., Avrett, E. H., & Loeser, R. 1981, ApJS, 45, 635
Wahlstrom, C., & Carlsson, M. 1994, ApJ, 433, 417
Warmuth, A., & Mann, G. 2020, A&A, 644, A172
Xu, Y., Cao, W., Ding, M., et al. 2016, ApJ, 819, 89
You, J. Q., & Oertel, G. K. 1992, ApJL, 389, L33
Zeng, Z., Qiu, J., Cao, W., & Judge, P. G. 2014, ApJ, 793, 87
Zhu, Y., Kowalski, A. F., Tian, H., et al. 2019, ApJ, 879, 19
Zirin, H. 1975, ApJL, 199, L63
Zirin, H. 1980, ApJ, 235, 618